

# Assessing the CO<sub>2</sub> emission reduction potential of steam cracking furnace innovations via computational fluid dynamics: from high-emissivity coatings, over coil modifications to firing control

*Florian Wéry<sup>1,‡</sup>, Moreno Geerts<sup>1,2,‡</sup>, Laurien A. Vandewalle<sup>1</sup>, Pieter A. Reyniers<sup>2</sup>, Geraldine J. Heynderickx<sup>1</sup>, Guy B. Marin<sup>1</sup>, Kevin M. Van Geem<sup>1\*</sup>*

<sup>1</sup>Laboratory for Chemical Technology (LCT), Ghent University, Technologiepark 125, B-9052 Ghent, Belgium.

<sup>2</sup>BASF Antwerpen, Scheldelaan 600, 2040 Antwerp, Belgium.

\*E-mail corresponding author: [Kevin.VanGeem@UGent.be](mailto:Kevin.VanGeem@UGent.be)

**Author Contributions:** The manuscript was written through contributions of all authors. All authors have given approval to the final version of the manuscript. ‡ Florian Wéry and Moreno Geerts contributed equally.

**Keywords:** Computational Fluid Dynamics, steam cracking, firebox efficiency, CO<sub>2</sub> emission, high-emissivity coating

**Abstract:** Accurate 3D modeling of steam cracking fireboxes is instrumental in the identification of the strengths and weaknesses of a specific firebox. A 3D computational fluid dynamics model for the firebox, combined with a 1D reactor model, is validated using industrial data of a naphtha steam cracker. The framework is used to assess the impact of a high-emissivity coating, geometrical changes and operational conditions on the CO<sub>2</sub> emissions per ton ethene produced. A high-emissivity coating reduces the CO<sub>2</sub> emissions by 4% and increases the radiation efficiency by 1.9%. A geometry with a higher number of inlets per reactor coil reduces the CO<sub>2</sub> emissions by 3%. When the excess oxygen concentration increases at the bridgewall, the firebox efficiency decreases while CO<sub>2</sub> emissions increase. The operational changes and technologies studied in this work can be combined to further minimize the CO<sub>2</sub> emissions, but controlling and monitoring the excess bridgewall oxygen proved to be the most crucial parameter to realize a reduction in CO<sub>2</sub> emissions.

# 1. Introduction

Ethene and propene are the most important chemical building blocks, with an annual production of over 300 million metric tons combined. With an increasing global population and rising living standards, this production is expected to increase during the coming decade, with steam cracking remaining the dominant means of olefin production [1, 2]. In order for alternative olefin production routes, such as natural gas- and renewable CO<sub>2</sub>-derived pathways, to compete with the mature steam cracking process, a feedstock price fall and significant process improvement is necessary [3, 4], which is unlikely to happen in the coming decade. Other innovations such as the electrification of steam cracking furnaces are promising; however, the required electricity needs to originate from renewable sources such as solar or wind which imposes a considerably long transition period [5].

A steam cracking unit consists out of 3 main parts: a convection section, a radiant section with the reactor coils located in the firebox, and a transfer-line exchanger (TLE). The hydrocarbon feedstock is mixed with steam before entering the convection section. In the convection section, the hydrocarbon mixture is heated by the hot flue gases exiting the radiant section. After this initial preheating, the hydrocarbon mixture is distributed over several reactor inlet tubes using venturis and fed into the radiant section. In this radiant section, the endothermic cracking reactions take place. This section is located in the firebox of the steam cracker, where numerous wall and/or floor burners supply the necessary heat to induce the endothermic reactions in the reactor tubes. After exiting the radiant section, the cracked gas is cooled down rapidly to around 600-750 K to stop the reactions in the process gas and prevent yield losses due to secondary reactions as much as possible. This is done in the TLE which in modern furnaces is located on top of the radiant section to minimize the residence time between the reactor and the quenching. This TLE is a heat-

exchanger in which the process gas is cooled on one side and boiler water is transformed to saturated high-pressure steam of around 120 bar on the other side.

Due to the temperatures of 1000-1200 K required to induce and sustain these reactions and the global olefin production volume, steam cracking is responsible for around 8% of the global chemical industry's energy consumption [6-8]. Typically, 1.2 and 1.8 kg of CO<sub>2</sub> per kg ethene produced is emitted during conventional ethane and naphtha steam cracking operation respectively, amounting to over 260 Mt of CO<sub>2</sub> emissions on a yearly basis [6]. In 2019, a total of 36.4 Gt of CO<sub>2</sub> was emitted worldwide, making steam cracking responsible for around 0.7% of this number, highlighting the huge potential in reducing the global CO<sub>2</sub> emissions via steam cracking process design [9].

Besides its energy requirement, the radiant section in the firebox of a steam cracking furnace is also the most maintenance-intensive part of the installation. During a run, coke is formed on the inside of the reactor coils and to a lesser extent in the TLE. This coke layer increases the heat transfer resistance, which raises the required heat duty towards the coil, consequentially increasing the tube metal temperature (TMT) in the firebox [10-12]. The growing coke layer also results in an increasing pressure drop over the reactor tubes. When either the TMT or pressure drop exceeds a critical value, the furnace must be shut down for decoking. The run length is defined as the time between two subsequent reactor decokes. Different measures can be taken to reduce coke formation, typically categorized into three groups: the introduction of feed additives such as sulfur containing compounds, mechanical structures enhancing heat transfer and doping of the reactor tube material, either at the surface via pretreatment operations or in the bulk during the tube production process [13-18].

Over time, the steam cracking process has been highly optimized, resulting in a well-established, mature technology. Although steam cracking is considered to be a mature technology, a lot of research is still ongoing, in particular to reduce coke formation and CO<sub>2</sub> emission reduction [19, 20]. The effect of different reactor coil designs on the coking rate was investigated numerically by Dedeyne et al. [21]. A swirl flow tube reactor was investigated both experimentally and numerically by Schietekat et al. showing its potential to enhance heat transfer to the process gas [22]. Vandewalle et al. performed dynamic computational fluid dynamics (CFD) simulations researching the impact of fouling on different reactor coil geometries [23]. The application of a high-emissivity coating to the refractory walls of steam cracking fireboxes improves the energy efficiency and reduces the CO<sub>2</sub> emissions of the global steam cracking process, as investigated both experimentally and numerically by Vangaever et al. [24, 25]. This last CFD study used a simplistic combustion model and did not include any validation data. More recently, wall burner designs were investigated numerically by Herce et al. [26]. Gong et al. focused on the entire steam cracker plant, including the downstream separation section, to increase the energy efficiency via high level energy efficiency integration optimization schemes [27]. A recent study by Mynko et al. investigated different revamp strategies of existing ethylene plants focused on CO<sub>2</sub> emission reduction via a life cycle assessment at a plant level, whereas the current work focuses on more detailed CFD simulations of a firebox and the effects within the firebox [28]. A biogas furnace and oxy-fuel combustion were said to be the technologies with the highest impact on the steam cracker's environmental footprint. Rebordinos et al. performed a CFD study similar to the present work on different measures to increase energy efficiency in a steam cracking firebox under different operating conditions [29]. However, the study by Rebordinos et al. is performed within a very different geometry and does not discuss changes to the product distribution of the firebox.

Modeling of both the fuel and process side of steam cracking fireboxes is often done via 0D or 1D models, which are fast to compute and are based on approximate heat fluxes towards the reactor coil. However, steam cracking fireboxes are far from uniform enough to be able to use such 0 or 1D models to accurately describe heat transfer. Amongst others the location of burners, the geometry of both coils and firebox, orientation of burner fuel tips and air supply are crucial parameters to be able to simulate heat transfer to the reactor tubes accurately [30]. CFD simulations are capable of representing all relevant phenomena occurring in a steam cracking firebox, provided that an appropriate grid and models are used [31, 32]. Due to the large size of the computational domain for steam cracking fireboxes and the wide spread in length scales, the computational cost associated with CFD modeling of fireboxes can be prohibitively high [33]. Therefore, accurate, computationally efficient models need to be implemented to ensure a reasonable computation time and to achieve a realistic view inside the steam cracking firebox simultaneously.

One approach to lower the computational cost of these CFD simulations, is via modeling the turbulent combustion inside the burners instead of solving a transport equation for each species in the fuel and oxidizer separately. A turbulent flame can be approximated by a wrinkled and distorted laminar flame, called a laminar flamelet. Instead of solving a transport equation for each species in the mixture, a transport equation is solved for the mixture fraction of this flamelet and its variance. Furthermore, a look-up table can be constructed in a pre-processing step to reduce the computational cost considerably. This method of modeling turbulent combustion is called flamelet modeling [33, 34].

In the temperature region at which the endothermic cracking reactions take place, radiation is the primary heat transfer mechanism. Over time, different radiation models have been developed for use in CFD simulations. Hottel developed a zone method for absorbing and emitting media

which divides the computational domain into several isothermal regions [35]. The view factor between each set of regions is then calculated allowing to determine the radiative heat flux between the different zones. With the increase in computational power, it now becomes feasible to solve the radiative transfer equation in each cell at each iteration. However, the zone method is still being applied in literature yielding satisfactory results in steam cracker CFD simulations [16, 36].

In this work, a firebox-reactor numerical framework is developed and validated against data coming from an industrial furnace. This numerical framework consists of a 3D CFD model to simulate the fuel side of the firebox while 1D reactor equations are solved for the process side in the reactor coils of the radiant. The impact on energy efficiency and the obtained product distribution of following adaptations to the firebox is assessed: a high-emissivity coating on the refractory walls, an alternative reactor geometry, and finally, the influence of the excess oxygen concentration as operational condition. The impact of these changes is assessed by evaluating among other things the reduction of the CO<sub>2</sub> emissions per ton ethene produced.

## 2. Mathematical models

### 2.1. Conservation equations

All firebox simulations are performed using the commercial CFD software package Ansys<sup>®</sup> FLUENT 19.0. In the fuel side of the firebox, the general conservation equations of mass, momentum, species and energy for a compressible fluid are solved using the finite volume method. These conservation equations when using flamelet modeling read as Eq. (1) to (5).

$$\frac{\partial \rho}{\partial t} + \vec{\nabla} \cdot (\rho \vec{u}) = 0 \quad (1)$$

$$\frac{\partial \rho Z}{\partial t} + \vec{\nabla} \cdot (\rho Z \vec{u}) = -\vec{\nabla} \cdot \vec{j}^Z \quad (2)$$

$$\frac{\partial \rho Z'}{\partial t} + \vec{\nabla} \cdot (\rho Z' \vec{u}) = \frac{\mu_t}{\sigma_t} \vec{\nabla} \cdot (\vec{\nabla} Z') + c_g \mu_t (\vec{\nabla} \cdot Z')^2 - c_x \rho \frac{\varepsilon}{k} Z'^2 \quad (3)$$

$$\frac{\partial \rho \vec{u}}{\partial t} + \vec{\nabla} \cdot (\rho \vec{u} \vec{u}) = -\vec{\nabla} p + \vec{\nabla} \cdot \bar{\tau} + \rho \vec{g} \quad (4)$$

$$\frac{\partial \rho H}{\partial t} + \vec{\nabla} \cdot (\rho H \vec{u}) = -\vec{\nabla} \cdot \vec{j}^H - \dot{q}_{rad} \quad (5)$$

In these equations,  $\rho$  represents density,  $t$  time,  $u$  velocity,  $p$  pressure,  $\bar{\tau}$  the viscous stress tensor,  $\mu$  the dynamic viscosity,  $\vec{g}$  the gravitational constant,  $Z$  the mixture mass fraction,  $Z'$  the mixture mass fraction variance,  $H$  the mean specific enthalpy,  $\vec{j}^H$  the enthalpy flux term and  $\dot{q}_{rad}$  the heat loss due to radiation.  $\sigma_t$ ,  $c_g$  and  $c_x$  are model constants with a value of 0.85, 2.86 and 2.0 respectively [37]. The continuity and momentum equations are coupled via the Semi-Implicit Method for Pressure-Linked Equation (SIMPLE). Since the flow is assumed to be Newtonian, the viscous stress tensor is expressed via Eq. (6) where  $\bar{I}$  is the unit tensor.

$$\bar{\tau} = (\mu + \mu_t) \left[ \vec{\nabla} \vec{u} + \vec{\nabla} \vec{u}^T - \frac{2}{3} (\vec{\nabla} \cdot \vec{u}) \bar{I} \right] \quad (6)$$

Due to the large dilution of the flue gas with nitrogen, the species flux  $\vec{j}^Z$  is modeled by Fick's law for species diffusion, see Eq. (7), instead of the Stefan-Maxwell equations for multi-component mixtures.

$$\vec{j}^Z = \rho D_z \vec{\nabla} Z \quad (7)$$

The enthalpy fluxes  $\vec{j}^H$  are accounted for using Fourier's law of heat conduction, given by Eq. (8).

$$\vec{j}^H = -k \vec{\nabla} T = -\frac{k}{C_p} \vec{\nabla} H \quad (8)$$

Due to the compressible nature of the flow resulting from non-negligible density variations, Favre-averaged values, i.e. density weighted averages, are used to account for the turbulent behavior instead of the standard Reynolds-averaged values, i.e. time weighted averages. Due to

this averaging, so-called Reynolds stresses appear in the momentum equations. In this work, the Re-Normalisation Group (RNG)  $k$ - $\varepsilon$  model is used to close the momentum equations [38].

## 2.2. Combustion model

The detailed GRI 3.0 kinetic network comprising of 53 species and 325 reactions is used to model the non-premixed combustion [39]. Due to the large scale of the firebox at hand, it is computationally impractical to model every ordinary differential equation (ODE) for all components in every cell at each timestep. Therefore, this mechanism is implemented in a tabulated way using non-adiabatic steady diffusion flamelet modeling.

Flamelet modeling uses 1D, counterflow diffusion flames, for which exact solutions can be calculated fast by specialized codes [40, 41]. Adiabatic 1D counterflow diffusion flames are characterized by two parameters: the mixture fraction,  $Z$ , and the scalar dissipation rate,  $\chi$ . The mixture fraction of this flamelet ranges between a value of 1 for a fuel-only mixture and 0 when the mixture is composed solely out of the oxidizer. The scalar dissipation rate is a measure for the straining of the flame which, for a 1D flame, increases by increasing the velocity of the fuel and oxidized jets or decreasing the distance between the jets. It is calculated via Eq. (9) in which  $\sim$  refers to the use of Favre-averaged values.

$$\chi = 2 \frac{\tilde{\varepsilon}}{\tilde{k}} \tilde{Z}^{\prime 2} \quad (9)$$

When the scalar dissipation rate goes to 0, the chemistry tends to equilibrium, whereas local quenching occurs when this value increases. When performing simulations under conditions with large influences of radiation, as observed in steam cracking fireboxes, an extra parameter needs to be included to account for the non-adiabatic cells: the enthalpy defect [42]. The enthalpy defect,  $\xi$ , is defined as the difference between the enthalpy of the calculated adiabatic flame,  $h$ , and the

real enthalpy in a certain cell, given by Eq. (10) with  $h_0$  and  $h_f$  the enthalpy of the oxidizer and fuel respectively.

$$\xi = h - [h_0 + Z(h_f - h_0)] \quad (10)$$

This difference is mainly caused by radiation in the internal and boundary cells and convective heat transfer at the boundary cells in these simulations. In the cases shown in this work, a pre-processing step generates a lookup table of these flamelets to be used during the CFD simulation based on mixture fractions, its variance and the enthalpy defect. Corresponding species concentrations and temperature are then obtained via lookup in this table during the calculation based on the prevailing conditions in the computational cell.

### 2.3. Radiation modeling

The Discrete Ordinates Model (DOM) is used to solve the radiation heat transfer throughout this work [43, 44]. The model uses and solves the radiative transfer equation (RTE), given by Eq. (11) under the assumption made here that scattering can be neglected.

$$\hat{s} \cdot \vec{\nabla} I_\lambda(r, \hat{s}) + \kappa_\lambda I_\lambda(r, \hat{s}) = \kappa_\lambda I_{b\lambda} \quad (11)$$

Herein,  $I_\lambda(r, \hat{s})$  represents the spectral intensity of wavelength  $\lambda$  at location  $r$  in direction  $\hat{s}$ ,  $\kappa_\lambda$  denotes the spectral absorption and  $I_{b\lambda}$  is the spectral black body intensity at wavelength  $\lambda$ . The first term of Eq. (11) represents the radiative intensity changes along a path in the direction  $\hat{s}$ . The second term models the decrease in intensity along the direction  $\hat{s}$  due to absorption by the participating gases. The term on the right-hand side accounts for the intensity by emission from the hot gas. In this work, each octant is discretized in 2 by 2 angular intervals.

Gas radiative properties, such as the absorption coefficient  $\kappa$ , are required to be able to solve the RTE for an absorbing-emitting gas mixture contained by opaque walls. The absorption coefficient contains millions of narrow spectral lines caused mainly by rotational and vibrational transitions

of gas species in the mixture. Heat transfer calculations using these lines are computationally unfeasible for combustions systems at the scale of industrial fireboxes due to the enormous amount of spectral evaluations of the RTE.

In order to reduce the necessary evaluations of the RTE, the weighted sum of gray gas models (WSGGM), developed by Smith, is used [45]. This model is capable of handling the effects of changes in flue gas composition, temperature and wall emissivity. The most important species to absorb and emit radiation in combustion applications are CO<sub>2</sub> and H<sub>2</sub>O. The WSGGM incorporates a clear band to be able to simulate the transparent regions in the electro-magnetic spectrum where no radiation is absorbed and emitted by the CO<sub>2</sub> and H<sub>2</sub>O molecules. This model replaces a real non-gray gas with N fictional gray gases, which all have a separate constant absorption coefficient  $\kappa_i$  and a temperature dependent weight factor  $a_i$ . Expressions for these parameters are those proposed by Smith [45, 46]. The total emissivity over a path length L is thus given by Eq. (12). In all cases presented here, a WSGGM consisting of four bands was used.

$$\varepsilon = \sum_{i=0}^{N-1} a_i(T)(1 - e^{-\kappa_i L}) \quad (12)$$

## 2.4. Reactor coil modeling

Ren et al. created a detailed free-radicals kinetic model for naphtha steam cracking based on automatic reaction network generation comprising of 1947 species and 82 130 reactions [47]. In reactive CFD simulations, a conservation equation for each species of the reaction network is solved. Solving the chemistry of a naphtha steam cracking reactor coil thus becomes impractical due to the excessive computational demand of solving over 1000 coupled ODE's per iteration. Therefore, the reactor simulation program COILSIM1D<sup>®</sup> is used in this work [48]. COILSIM1D<sup>®</sup> efficiently combines a single-event micro-kinetic model with 1D reactor equations, allowing to perform reactor simulations including a large amount of species within seconds. Because of the

high Reynolds numbers inside the reactor coils, radial gradients can be neglected, allowing to accept the assumption of plug flow [49, 50].

Due to the non-isothermal, non-adiabatic and non-isobaric nature of steam cracking, the reactor model consists of conservation equations for mass, momentum and energy, shown in Eq. (13) to (15) respectively.

$$\frac{dF_i}{dz} = R_i A \quad (13)$$

$$\sum_i F_i \cdot C_{p,m,i} \cdot \frac{dT}{dz} = \omega \dot{q} + A \left( \sum_i R_i h_i \right) \quad (14)$$

$$-\frac{dp_t}{dz} = \left( \frac{2f}{d_t} + \frac{\zeta}{\pi r_b} \right) \rho_g u^2 + \rho_g u \frac{du}{dz} \quad (15)$$

In Eq. (13),  $F_i$  represents the molar flow rate of component  $i$ ,  $z$  the axial position,  $R_i$  the net rate of production for component  $i$  and  $A$  the tubes cross-sectional surface area.  $\dot{q}$  represents the heat flux to the process gas,  $h_i$  the partial molar enthalpy of species  $i$ ,  $T$  the temperature,  $\Delta_f H_i$  the enthalpy of formation of component  $i$ ,  $C_{p,m,i}$  the molar heat capacity of component  $i$  at temperature  $T$ ,  $\omega$  the circumference of the reactor in Eq. (14). In Eq. (15),  $p_t$  represents the total pressure,  $f$  the Fanning friction factor,  $d_t$  the diameter of the reactor tube,  $r_b$  the radius of the U-turn of the reactor,  $\zeta$  the Nekrasov factor for bends,  $\rho$  the density and  $u$  the velocity of the flow in the reactor.

The kinetic model used in COILSIM1D<sup>®</sup> consists of 956 species, 109 radicals and over 4 000 reactions [48, 49]. The reaction rate coefficients are calculated using a group contribution method developed by Sabbe et al. [51]. For each reaction family, a reference reaction is defined. This reference reaction is then used as the basis on which perturbation terms are added, depending on the specific structure of the species involved.

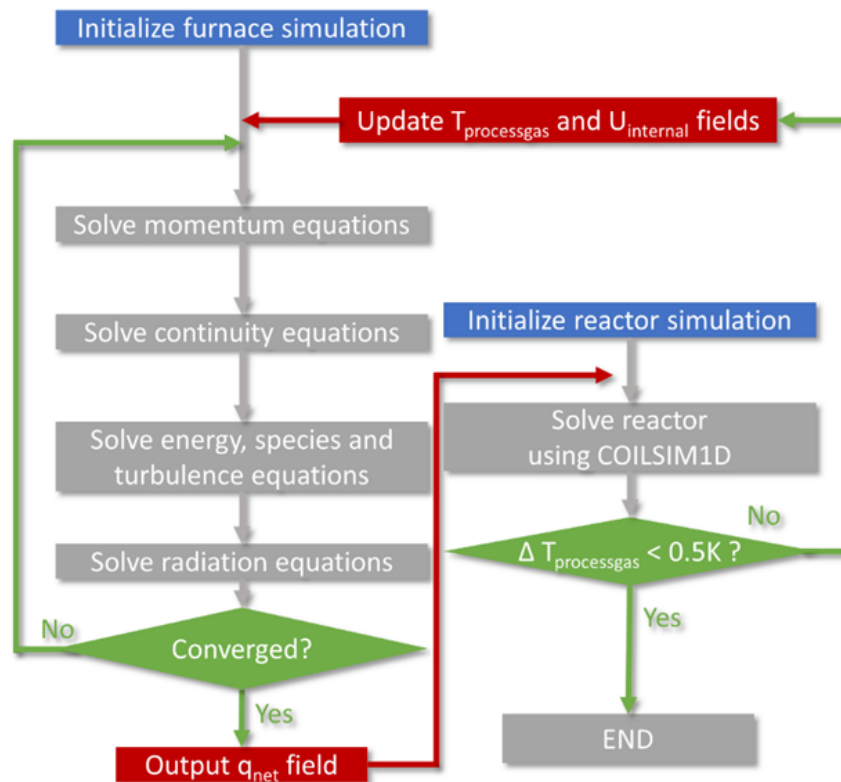
In order to simulate the run length of the firebox, a coking rate is calculated by COILSIM1D<sup>®</sup> based on the start-of-run incident radiative heat flux (IRHF) on the reactor coil obtained out of the CFD simulations, as described by Zhang et al. [52]. The coking rate,  $r_c$ , at each axial position in the reactor is determined using the semi-empirical equation derived by Plehiers et al. [53]. In these run length simulations, the coking rate is assumed to be identical over the entire COILSIM1D<sup>®</sup> timestep, after which additional coke is added to the coke layer. This coke layer introduces an additional heat transfer resistance which reduces the heat transferred to the process gas. To compensate, the IRHF profile is scaled to maintain an identical cracking severity at the reactor coil outlet, hereby increasing the required firing rate and TMT's. The propene to ethene ratio (P/E) can be defined as a measure for the cracking severity. This ratio decreases with a higher cracking severity, i.e. with more intense cracking. After updating the IRHF profile and TMT's, a new simulation is started at the next point in time. The timestep imposed in the run length simulations is 24 hours, in line with previous work [23].

## 2.5. Firebox-reactor coil coupling

The 3D-1D firebox-reactor coil coupling used in this work is represented in Scheme 1. The CFD furnace simulation is initialized using an initial guess of the process gas temperature and internal heat transfer coefficient,  $U_{internal}$ , obtained from preliminary 1D reactor coil simulations within COILSIM1D<sup>®</sup>. This internal heat transfer coefficient contains the contribution of convective heat transfer from the process gas to the internal wall and conductive heat transfer through the tube wall. The process gas temperature and the internal heat transfer coefficient are then imposed as a boundary condition in the CFD simulation. More information regarding the calculation of  $U_{internal}$  and the coupling with FLUENT is provided in Supporting Information. FLUENT then accounts for convective heat transfer between the outer wall of the reactor coil and the flue gas.

The firebox is simulated until the bridgewall temperature, i.e. the temperature of the flue gas leaving the radiant section, changes less than 1 K over 1000 subsequent iterations in the CFD framework. The circumferentially averaged net heat flux is then extracted from the 3D firebox simulation and imposed on a new 1D reactor coil. The 1D reactor coil simulation then returns a process gas temperature and internal heat transfer coefficient profile, which are in turn imposed when repeating the CFD firebox simulation. This iterative process is continued until the maximum change in process gas temperature between iterations is less than 0.5 K at each axial position in the tube.

**Scheme 1.** Flow diagram of the firebox simulations performed in this work.



Using the process gas temperature and corresponding global heat transfer coefficient profiles from the 1D simulation in the 3D CFD simulation results in the possibility to also see differences in TMT along the circumference of the reactor coils. This is important to be able to verify radiation

shadow effects in steam cracking fireboxes [54]. Additionally, this way of coupling results in a reduced amount of needed firebox-reactor coil iterations, no more than 3, due to the less severe changes in process gas temperatures compared to the TMT's.

### 3. Simulation set-up

A schematic representation of the firebox simulated in this work is shown in Figure 1. The base geometry will be discussed here while adaptations will be explained in their corresponding sections. One coil consists of five parallel first passes which are connected to a second pass via a manifold at the bottom of the firebox. The first passes are smaller in diameter than the second pass to increase the available surface area for heat transfer. The second pass has a larger diameter to minimize the pressure drop increase in this high-temperature, high coking rate region of the coil. The manifold is located in a trough at the bottom of the firebox, below the elevation of the floor burners to shield it from direct radiation. The full firebox holds 12 coils in groups of 4. Each group of 4 coils is connected to one transfer-line exchanger (TLE). Due to rotational symmetry along the center of the firebox, only one sixth of the firebox, i.e., the region between the dashed lines in Figure 1b, is simulated to avoid excessive computational effort. This one sixth encompasses 2 coils and 4 floor burners, also shown in Figure 1. The boundary conditions along the edge planes of this one sixth of the geometry account for the rotational symmetry, i.e. gas leaving via the top left side of the left plane shown in Figure 1, located close to an outlet tube, is introduced via the bottom left side. Since the flue gas flow is dominated by its axial component, any error introduced via this discretization of the geometry is assumed to be negligible compared to the extra computational cost related to simulating the complete firebox.

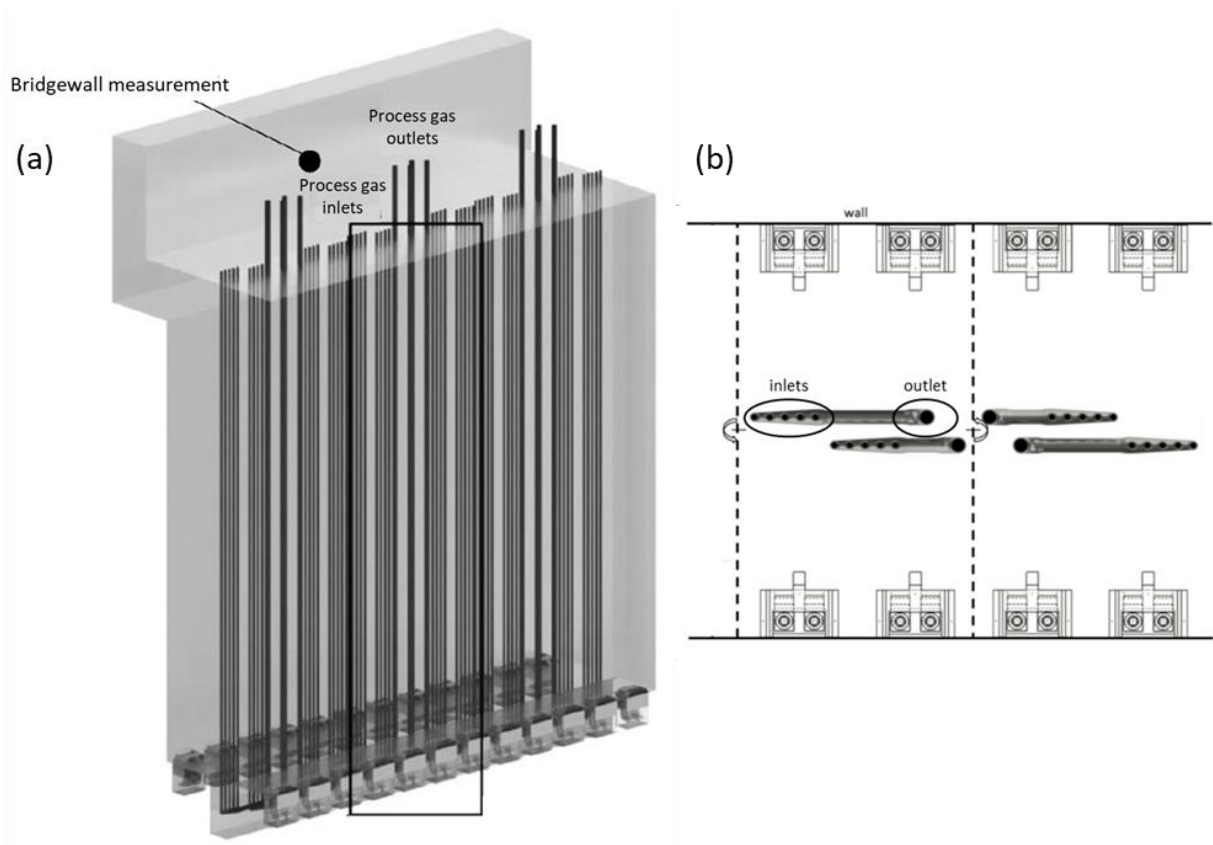


**Figure 1.** (a) View of the complete firebox showing the location of the bridgewall measurement point. The black rectangle indicates 1/3<sup>rd</sup> of the firebox, shown in (b), which is connected to one TLE. Due to rotational symmetry, half of this region, i.e. the region between the dashed lines, is considered in the 3D CFD simulations.

Because the effect of burner arrangement and its geometry is critical, the burner geometry is considered in detail. The mesh is very fine around the burner tips to be able to simulate the high concentration and temperature gradient regions while being coarser at the top of the firebox. Refinement at the top of the firebox is unnecessary since gradients are significantly smaller there compared to the flame region at the bottom of the firebox. Due to this large spread in relevant dimensions over the firebox, a stepwise octree refinement method is used to discretize the computational domain. Using both the OpenFOAM cell snapping tool snappyHexMesh and

FLUENT's built-in adaptive mesh refining tool, a range of refinements is imposed. Figure 2 shows local mesh refinement around the floor burners. Distinct refinements are present near the fuel tips and in the region of the firebox in which the fuel is injected. Each fuel tip has one main outlet pointed upwards and several smaller outlets directed towards the air ducts, which explains the additional refinement from the fuel tip to the air ducts on Figure 2b. The final mesh comprises of 15.4 million hexahedral cells. All relevant geometric features and operating conditions corresponding to the base geometry are given in Table 1. A detailed PIONA analysis of the naphtha feedstock is given in Table 2. A mesh independence study is performed where the cells of the aforementioned mesh are further refined based on the temperature gradient obtained at steady state. The temperature gradient is chosen since the temperature field and corresponding heat flux towards the coils predominantly determine the outlet composition of the steam cracking reactor coils. Regions with the highest temperature gradient show the largest change in gas composition. A global cell size reduction would not have a large impact on these regions due to the size of the complete geometry and the lesser effect of cell size in the upper regions of the firebox. The bridgewall temperature is monitored until a new steady state is reached. After refinement, two new meshes are obtained with cell counts of 19.5 and 24.4 million cells respectively. The bridgewall temperatures at steady-state for the meshes consisting of 15.4, 19.5 and 24.4 million cells are 1416, 1416 and 1417 K respectively. Since the bridgewall temperature remains almost constant in all three meshes, adequate resolution is obtained already in the coarsest considered mesh.

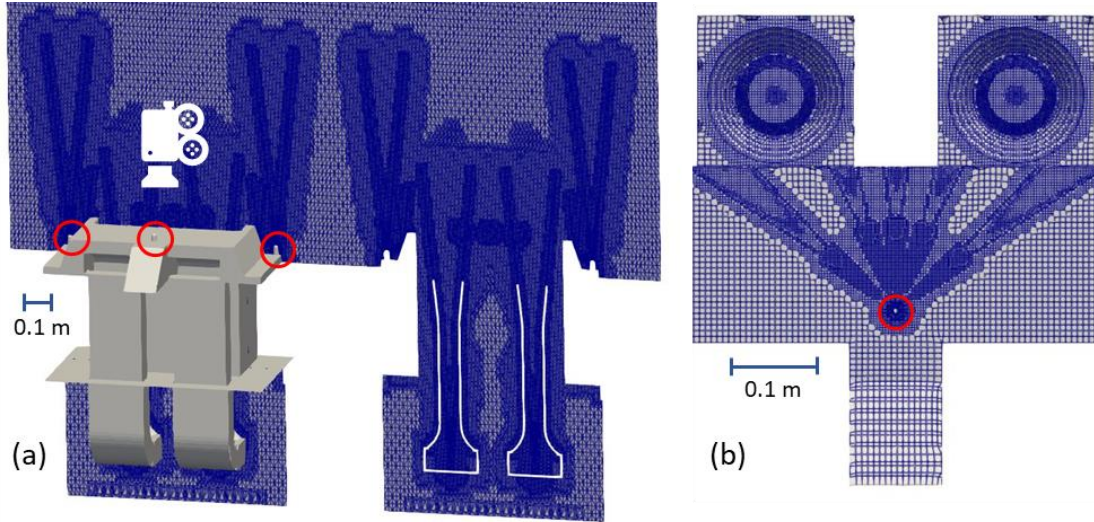


**Figure 2.** (a) Mesh refinement near the floor burners and (b) a top-view of the floor burner mesh. Fuel tips are indicated in red.

**Table 1.** Geometric characteristics of the firebox and operating conditions.

<b>Simulated firebox dimensions</b>	
Length (m)	2.32
Width (m)	4.08
Height (m)	14.41
<b>Firing conditions</b>	
Fuel flow rate per burner (kg/s)	0.0501
Air flow rate per burner (kg/s)	0.982
Air equivalence ratio	1.11
Fuel/air inlet temperature (K)	300
Firebox outlet pressure (Pa)	101 325
<b>Fuel composition</b>	
CH <sub>4</sub> (wt%)	96.7
H <sub>2</sub> (wt%)	2.5

C <sub>2</sub> H <sub>4</sub> (wt%)	0.8
<b>Operating conditions</b>	
Steam dilution (kg <sub>H<sub>2</sub>O</sub> /kg <sub>HC</sub> )	0.4
Coil inlet temperature (CIT) (K)	898
Coil outlet pressure (Pa)	297 000
Severity index: C <sub>3=</sub> /C <sub>2=</sub>	0.705
<b>Material properties</b>	
Firebox refractory emissivity	0.5
Coil tube skin emissivity	0.9
<b>Reactor coil dimensions</b>	
Number of passes	2
Number of inlets 1 <sup>st</sup> pass	5
Number of outlets 2 <sup>nd</sup> pass	1
Wall thickness (m)	0.00675
Total coil length (m)	34.65

**Table 2.** Detailed PIONA analysis of the naphtha feedstock

	<b>n-Paraffins (wt%)</b>	<b>i-Paraffins (wt%)</b>	<b>Olefins (wt%)</b>	<b>Naphthenes (wt%)</b>	<b>Aromatics (wt%)</b>
<b>C<sub>4</sub></b>	2.03	0.38	0.00	0.00	0.00
<b>C<sub>5</sub></b>	10.94	7.32	0.00	1.08	0.00
<b>C<sub>6</sub></b>	10.00	10.79	0.00	6.53	1.38
<b>C<sub>7</sub></b>	5.17	9.98	0.00	11.35	1.52
<b>C<sub>8</sub></b>	2.75	3.38	0.00	4.02	1.60
<b>C<sub>9</sub></b>	1.57	2.70	0.00	2.21	1.22
<b>C<sub>10</sub></b>	0.57	1.49	0.00	0.00	0.00

## 4. Results and discussion

### 4.1. Validation study

The computational model is validated using the industrial plant data given in Table 3. The naphtha composition and flow rate, fuel composition and flow rate, CIT and coil inlet pressure (CIP) are used as fixed boundary conditions. The outlet plane of the firebox is defined as an empty plane, implying the emissivity equals 1. Additionally, the industrial oxygen concentration measured at the bridgewall is used to calculate the air flow towards the burners. This is achieved through a preliminary iterative procedure by varying the air equivalence ratio until the desired excess oxygen concentration is reached. This means the coil outlet temperature (COT), the P/E ratio, flue gas bridgewall temperature (BWT) and maximum TMT remain available for validation purposes.

As shown in Table 3, the simulated COT, P/E and BWT are close to the measured values, with deviations of less than 2%. The P/E is the most reliable measurement and is more sensitive to operational changes than for example the COT. Since the calculated P/E is in perfect agreement with the measured one, this is a strong indication that the simulation framework can accurately describe the overall effects occurring in a steam cracking firebox. Minor deviations can be observed for the remaining industrial data. These are well within the uncertainty of these measurements.

Free thermosiphon operation is assumed for the TLE, implying that the mass flow on the water-steam sides is determined by buoyancy and natural convection. The one-dimensional conservation equations for species, momentum, and energy as described in section 2.3 are used to simulate the process side of the TLE. Therefore, additional reaction is considered during the cooling of the process gas. The boundary condition on the water/steam side is set to a fixed temperature, corresponding to the saturation temperature of water at the considered pressure of 120 bar.

**Table 3.** Comparison between industrial data and the obtained simulated data with operating conditions specified in Table 1. The validating measurements are indicated in bold.

	<b>Measurement</b>	<b>Simulation</b>	<b>Rel. dev. [%]</b>
CIT [K]	898	898	-
<b>BWT [K]</b>	<b>1390</b>	<b>1416</b>	<b>+ 1.87</b>
<b>COT [K]</b>	<b>1070</b>	<b>1081</b>	<b>+ 1.03</b>
P/E after coil	/	0.713	-
<b>P/E after TLE</b>	<b>0.705</b>	<b>0.705</b>	<b>± 0.00</b>
<b>Maximal TMT [K]</b>	<b>1278</b>	<b>1285</b>	<b>+ 0.55</b>
O <sub>2</sub> BW [vol%]	1.9	1.9	-

The thermocouple on the industrial furnace measuring the BWT is located in a region where the temperature is approximately 10 K lower compared to the area-averaged flue gas temperature at that height, as shown in Figure 3. The area-weighted averaged value of the exiting flue gas is reported rather than the temperature at the measurement location since this is the most accurate value for efficiency calculations.

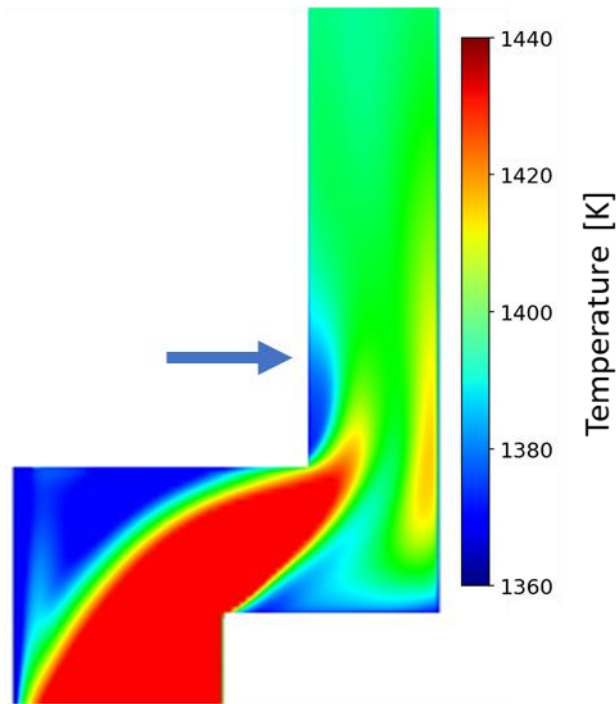


**Figure 3.** Local temperature profile near the outlet of the firebox for the validation case. The location of the bridgewall measuring point is indicated via the blue arrow.

The overshoot in TMT can be related to the accuracy of the industrial measurement, obtained via a pyrometer. Since the emissivity of the reactor coil is not 1, a difference arises in the measured and real temperature. Secondly, the pyrometer might not be pointed at the exact spot of the maximum TMT.

The calculated COT is about 10 K higher than the COT of the plant data. First of all, the thermocouple measures the COT at the center of the coil outlet instead of measuring the cross-sectional averaged temperature. Imperfect outward insulation of the thermocouple and its thermowell could also decrease the measured COT.

However, since the P/E ratio is perfectly aligned, and all other small deviations can be explained by imperfections in measurements techniques, the computational framework can be considered

validated and used to optimize the firebox. In the following paragraphs, the influence of a high-emissivity coating, reactor geometry and excess O<sub>2</sub> concentrations are discussed to demonstrate the capabilities of the developed computational model in helping to decide how CO<sub>2</sub> emissions can be cost-effectively reduced.

#### 4.2. Influence of high-emissivity coating

High-emissivity coatings are designed to increase the radiative flux from the firebox to the reactor coils. These coatings increase the emissivity of the refractory walls and/or reactor coils to emit and absorb more radiation, with as net result a higher heat flux towards the reactor coils. The influence of this effect strongly depends on the geometry of the firebox and the coils. In this section, the influence of applying a high-emissivity coating to the walls of the considered firebox is investigated. The wall refractory emissivity is increased from 0.5 to 0.95. The value for the base case is obtained as an average from previous work [55], whereas the increased value is taken as an upper limit of the achievable emissivity using coatings [24, 25].

The results of two different simulations with increased wall refractory emissivity are presented in Table 4. In the first, called case A, the fuel flow rate as well as the CIT are kept constant compared to the base case. In the second, called case B, the fuel flow rate is lowered to achieve a similar P/E ratio as the base case.

**Table 4.** Comparison between base case ( $\varepsilon = 0.5$ ), case A ( $\varepsilon = 0.95$ ) and case B ( $\varepsilon = 0.95$  with 96% of original fuel flow rate) [other operating conditions shown in Table 1].

	<b>Base Case</b>	<b>Case A</b>	<b>Case B</b>
BWT [K]	1416	1396	1384
COT [K]	1081	1090	1081
P/E after coil	0.713	0.681	0.712

P/E after TLE	0.705	0.674	0.708
TMT <sub>max</sub> [K]	1285	1295	1291
O <sub>2</sub> BW [vol%]	1.9	1.9	1.9
Firebox efficiency [%]	42.6	44.4	44.5
CO <sub>2</sub> /C <sub>2</sub> H <sub>4</sub> [kg/kg]	1.22	1.17	1.18

For reasons of comparison, the firebox efficiency,  $\eta_{firebox}$ , is calculated via Eq. (16). Herein,  $\dot{Q}_{in}$  and  $\dot{Q}_{out}$  denote the total heat transfer rate via the furnace in- and outlets,  $\dot{Q}_{combustion}$  the total thermal power released by the combustion and  $\dot{Q}_{reactor}$  the total heat transfer rate towards the reactor coils. However, it must be noted that the full furnace efficiency is significantly higher than this firebox efficiency due to the incorporation of the convection section in a steam cracking unit.

$$\eta_{firebox} = 1 - \frac{\dot{Q}_{out} - \dot{Q}_{in}}{\dot{Q}_{combustion}} = \frac{\dot{Q}_{reactor}}{\dot{Q}_{combustion}} \quad (16)$$

When the fuel flow rate is kept constant, i.e. case A, a 21 K decrease in flue gas bridgewall temperature is observed. This is the result of the increased heat transfer efficiency of 1.8% towards the process gas. The firebox efficiency increases from 42.6% to 44.4% resulting in an increase of the COT by approximately 10 K. This also increases the cracking severity, as shown by the decreasing P/E ratio from 0.705 to 0.674.

However, the downside of this increased heat transfer is an increase of the maximum TMT by 14 K. This can be partially compensated by reducing the fuel flow rate to the firebox.

In case B, the fuel and corresponding air flow rates are reduced to 96% of the base case value such that the same P/E as the non-coated case is achieved. This implies that the firebox needs 4% less fuel when applying a high-emissivity coating and thus reducing the CO<sub>2</sub> emissions per kg ethene by around 4% as well. Due to the more efficient heat transfer and the lower upwards

momentum of the flue gas due to the lower fuel flow rate, there will be less power available in the convection section, shown by a decrease of 32 K in BWT compared to the base case. By producing less or lower temperature high-pressure steam in the convection section the coil inlet temperature can be kept approximately the same. An alternative option is to lower the coil inlet temperature. This reduction in CIT in turn results in the need to transfer more heat to the coils in the firebox by burning more fuel, thus reducing the firebox efficiency gain obtained by the high-emissivity coating, making the 4% CO<sub>2</sub> emission reduction a best-case scenario.

There is a small but significant shift in the incident radiative heat flux towards the coils, as displayed in Figure 4. The high-emissivity case produces a 2% higher flux peak on both tube passes compared to the base case with a slightly lower heat flux in the top of the firebox. This implies that the top 6 m of the firebox gets a little less heat while the bottom and intermediate parts get a little more, resulting in the 6 K higher maximum TMT for case B. The origin of this heat flux peak is related to the increased heat transfer from the furnace walls to the coils.

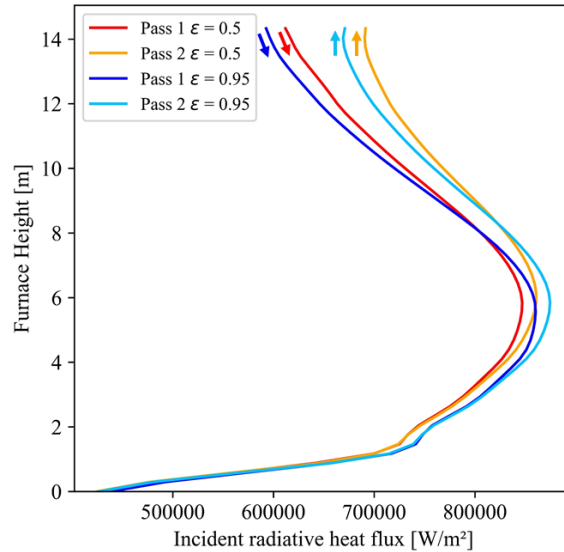


**Figure 4.** Comparison of the base case ( $\varepsilon = 0.5$ ) and case B of the circumferentially averaged incident radiative heat flux towards the coils versus the firebox height, other operating conditions shown in Table 1. Arrows indicate the flow direction.

The influence of applying a coating to the furnace walls on the run length is evaluated by plugging the IRHF profile obtained by the CFD simulations into COILSIM1D<sup>®</sup>. This higher peak IRHF and corresponding TMT results in a decrease in run length by 11.3%. However, the better radiative heat transfer results in a 4% decrease in kg CO<sub>2</sub> per kg ethene produced as discussed above. Due to this complex interplay, a thorough economic and ecologic evaluation needs to be made to determine the relative importance of a firebox efficiency increase and less flue gas heating power available in the convection section compared to a loss in run length.

### 4.3. Influence of reactor geometry

The original reactor geometry has 3 TLE's, each with a set of 4 reactor coils each composed of 5 first passes connected to one second pass. Therefore, the base case will be referred to as the '20-4' configuration, referring to 20 inlet and 4 outlet tubes per TLE, hereafter. To increase the run-

length of the furnace, it is proposed here to increase the number of inlets, hereby increasing the surface area available for heat transfer towards the process gas in the first pass. A design with 8 smaller diameter inlets is assessed in this section, referred to as the ‘32-4’ configuration. This configuration was meshed with identical refinement compared to the base case. The smaller inlet tube diameters of the ‘32-4’ configuration allow for an increase of the available heat transfer area by 42% while increasing the cross-sectional flow area by 26%.

Due to the increased number of inlet slots, a grouped inlet configuration as shown on Figure 1 is rejected due to the limited space between 2 adjoining inlets. Therefore, a staggered configuration is proposed. This staggering causes additional shadow effects giving rise to larger TMT differences around the circumference of the tubes, possibly resulting in bending of tubes due to the increased thermal stresses. Simulation results of the ‘32-4’ configuration with the same fuel flow rate as the base case and of the ‘32-4’ configuration where the fuel flow rate is adjusted to achieve identical cracking severity are gathered in Table 5. To achieve an identical cracking severity, 3% less fuel is needed compared to the ‘20-4’ configuration, resulting in an approximately 3% reduction in CO<sub>2</sub> emissions per kg of ethene produced.

**Table 5.** Results comparison between ‘20-4’ and ‘32-4’ configurations [other operating conditions shown in Table 1].

	<b>Base Case ‘20-4’</b>	<b>‘32-4’</b>	<b>‘32-4’ 97% fuel</b>
BWT [K]	1416	1369	1358
CIT [K]	898	878	873
COT [K]	1081	1085	1078
P/E after coil	0.713	0.69	0.717

P/E after TLE	0.705	0.685	0.71
TMT <sub>max</sub> first pass [K]	1274	1280	1274
TMT <sub>max</sub> second pass [K]	1285	1271	1273
O <sub>2</sub> BW [vol%]	1.9	1.9	1.9
Firebox efficiency [%]	42.6	45.7	46.0
CO <sub>2</sub> /C <sub>2</sub> H <sub>4</sub> [kg/kg]	1.22	1.20	1.19

Due to the increased surface area on the reactor's first passes, the total amount of heat transferred to the process gas is expected to increase when using the same fuel flow rate to the furnace. Consequently, the flue gas bridgewall temperature is expected to decrease significantly. This decreased BWT will cause a decreased CIT due to the reduced power to heat the feedstock in the convection section. Based on similar characteristics in the industrial data of the firebox, a drop in CIT of 25 K from 898 K to 873 K due to the lower BWT is assumed. A lower firing rate further decreases the BWT, which caused an additional drop of 5 K in CIT. Further discussions will only consider a comparison between the '20-4' configuration and the '32-4' configuration with reduced firing rate.

The circumferentially averaged incident radiative heat fluxes are given in Figure 5 for both the base case and the '32-4' configuration to which 97% of the original fuel flow rate is fed. When comparing both geometries, a 12 and 8% higher heat flux peak is obtained on the first and second pass of the '20-4' configuration compared to pass 1 and pass 2 of the '32-4' configuration respectively. The increase in peak heat flux between the first and the second passes in the '32-4' geometry is significantly higher compared to the '20-4' geometry, with values of 6 and 2% respectively. These lower heat fluxes towards the coil in the '32-4' configuration and this larger difference in peak heat flux between the first and second pass stem from the increase in surface

area available for radiative heat transfer. This increased surface area also results in an increased firebox efficiency, i.e. 46.0% versus 42.6% for the ‘32-4’ and ‘20-4’ geometries respectively.

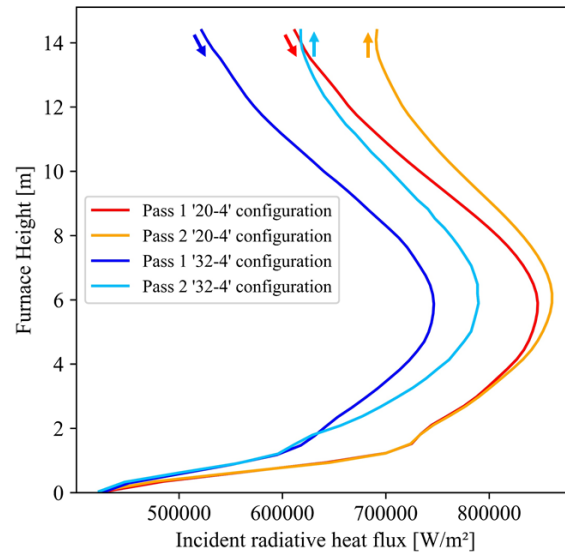


**Figure 5.** Influence of reactor design on circumferentially averaged incident radiative heat flux versus furnace height, other operating conditions shown in Table 1. Arrows indicate the flow direction.

A schematic view of the cold and hot TMT spots is shown in Figure 6. When analyzing the circumferential differences in TMT’s, a peak difference of 95 K is observed for the ‘32-4’ configurations compared to 75 K for the ‘20-4’ base case. The location of these minimum and maximum TMT’s also differs. The ‘20-4’ case has its lowest TMT’s at the center of the tubes while the highest and lowest TMT’s for the ‘32-4’ configuration are located at the opposite side of the reactor tube, resulting in an overall comparable circumferential temperature gradient in both cases. As the temperature gradient and its corresponding difference in thermal expansion is the most important factor for thermal stresses, it is expected that the ‘32-4’ configuration would not pose any significant problems compared to the ‘20-4’ configuration. However, bending of the

tubes could be more pronounced due to the opposite position of the so-called sunny and shady sides of the reactor tubes. This could result in a longer reactor elongation at the fire side compared to the colder side and thus a more bended tube than tubes in the ‘20-4’ configuration.

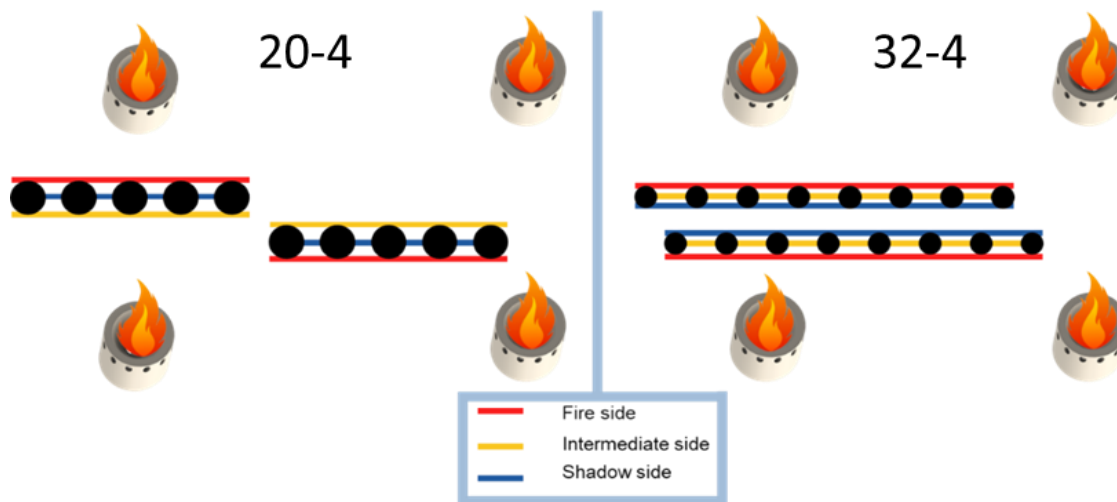


**Figure 6.** Schematic representation of the sunny and shady side of the inlets for the ‘20-4’ and ‘32-4’ reactor configurations.

Due to the increase in available cross-sectional area in the ‘32-4’ configuration, the pressure drop over the reactor coil is lowered by 15%, from 0.453 bar for the ‘20-4’ geometry to 0.384 bar. However, with the increased cross-sectional area, the residence time also increases with 15%, resulting in more secondary reactions. The ethene, propene and 1,3-butadiene yields decrease by 0.6%, 0.1% and 0.9% respectively, relative to the ‘20-4’ reactor configuration. The benzene, toluene and xylene yields increase by 0.7%, 1.9% and 2.6% respectively, relative to the ‘20-4’ case. This increase in BTX yields implies a yield increase in heavier aromatics, which can condense in the TLE, increasing the fouling rate in this part of the reactor.

Finally, the impact on the run length of all influences described above is assessed. This yields an increase in run length of 82%, primarily due to the 8% lower peak IRHF on the second pass of the ‘32-4’ reactor geometry.

#### 4.4. Influence of flue gas excess oxygen concentration

New technological options like high-emissivity coatings as discussed above are not the only way to improve the steam cracking firebox performance. Operational conditions can also increase both throughput and efficiency. One of the main handles to work with in an industrial steam cracking firebox is the air flow rate. In some fireboxes, the flames are inspected visually and the air registers to the burners are opened or closed manually accordingly. Automatic control of the air flow rate can be achieved by measuring the stack or bridgewall O<sub>2</sub> or CO concentration. As CO is an indication of incomplete combustion, the formation of CO needs to be avoided to reduce the significant safety risks associated with the buildup of combustible species in a confined space.

Induced-draft fireboxes can be regulated to a given stack O<sub>2</sub> concentration by altering the speed of the stack fan, thus creating a slightly higher or lower vacuum that results in an increased O<sub>2</sub> concentration. In a forced draft firebox, the air intake can be increased by increasing the air compressor flow rate.

Next to the base case where a bridgewall oxygen concentration of 1.9 vol% is maintained due to the air equivalence ratio of 1.11, a simulation with a bridgewall oxygen concentration of 2.8 vol% is performed. The 1.9 vol% and 2.8 vol% excess O<sub>2</sub> concentration at the bridgewall correspond to around 11 and 17% excess air compared to stoichiometric combustion of the flue gas. These excess oxygen values are realistic values since both have been measured in an industrial firebox and since typical gas-fired fireboxes and boilers are designed for about 10 to 15% excess combustion air. However, the air flow rates are often significantly higher than the design values due to operational safety considerations or tramp air. This simulation requires an additional 5.5% combustion air compared to the base case, for the fuel composition listed in Table 1. Both simulations are performed to achieve the same P/E ratio of 0.705 after the TLE. To achieve this desired cracking

severity, the fuel flow rate of the excess oxygen case needs to be increased by 6.4% compared to the base case. Results of both simulations are given in Table 6.

**Table 6.** Influence of increasing the excess oxygen concentration on the main furnace performance indicators [other operating conditions shown in Table 1].

	<b>Base Case 1.9 vol% O<sub>2</sub></b>	<b>2.8 vol% O<sub>2</sub></b>	<b>Rel. dev. [%]</b>
BWT [K]	1416	1422	+ 0.4
Fuel gas flow rate [kg/s]	0.2004	0.2132	+ 6.4
Flue gas velocity [m/s]	5.61	6.26	+ 11.6
Firebox efficiency [%]	42.6	40.2	- 5.6
CO <sub>2</sub> /CH <sub>4</sub> [kg/kg]	1.22	1.30	+ 6.5

The main performance indicators to be examined by changing the excess oxygen concentration are the firebox efficiency and the CO<sub>2</sub> emissions per ton ethene produced. The firebox efficiency is seen to decrease from 42.6% to 40.2% by increasing the excess O<sub>2</sub> concentration from 1.9 vol% to 2.8 vol% shown by an increase in BWT of 6 K.

The firebox flue gas outlet temperature remains similar in both cases, while the needed fuel flow rate increases with 6.4%. Due to the additional air flow rate needed for the extra fuel and higher excess oxygen concentration, the flue gas velocity also increases significantly by 11.6%. The additional fuel needed also results in an increased amount of CO<sub>2</sub> emissions per ton ethene produced, 6.5% higher compared to the base case. This is clearly a very significant impact and therefore the excess O<sub>2</sub> should always be strictly monitored when operating a steam cracking firebox. However, due to the higher flue gas flow rate, a higher amount of heat duty is available for preheating the process gas and steam generation in the convection section. This results in a

higher CIT that what has been imposed now. Therefore, the 6.5% increase in CO<sub>2</sub> emissions is a worst-case scenario overestimating the actual performance decrease.

The calculated incident radiative heat fluxes from the firebox to the coil are displayed in Figure 7. There is a very minor shift of the heat flux peak towards a higher position in the firebox for the case higher in excess oxygen concentration. Also, the IRHF peak is 0.4% lower and slightly more heat is transferred to the reactor coil at the top of the firebox. This is related to the increased upwards momentum of the flue gas due to the increased air and fuel flow rates. However, this is far less pronounced compared to the previously examined wall emissivity change. This means that the heat transfer in the firebox does not significantly depend on the increased flue gas flow rate in the examined operational window since the impact of higher fuel flow rate is countered by the higher concentration of excess oxygen.

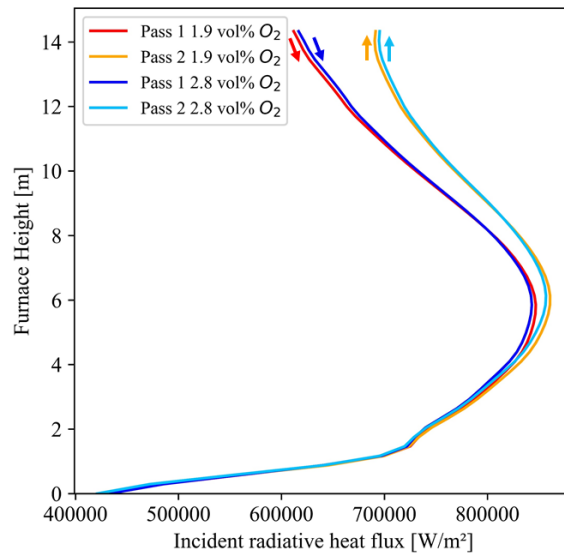


**Figure 7.** Influence of oxygen concentration at the bridgewall of the firebox on circumferentially averaged incident radiative heat fluxes, other operating conditions shown in Table 1. Arrows indicate the flow direction.

## 5. Conclusions

A computational 3D-1D firebox-reactor coil simulation framework is set up coupling Ansys® FLUENT and COILSIM1D®. This framework is then validated against industrial furnace data. Excellent agreement for different performance indicators such as the coil outlet temperature and the propene to ethene ratio is obtained. The validated framework is used to assess the influence of applying a high-emissivity coating, inserting a different reactor geometry and changing the excess bridgewall oxygen concentration. From all these modifications, the excess bridgewall oxygen concentration seems to have the strongest impact on the CO<sub>2</sub> emissions of the furnace, followed by the use of a high-emissivity coating on the refractory and finally the reactor geometry. Applying a high-emissivity coating on the refractory walls reduces the CO<sub>2</sub> per kg of ethene by 4% when the same cracking severity is upheld. However, due to the increased emissivity, the flame is slightly more compact, resulting in a higher heat flux peak, and a slightly lower heat flux in the top of the firebox. Additionally, the tube metal temperature slightly increases at start-of-run conditions, reducing the furnace run length by 11.3%.

Inserting an alternative reactor design with 8 smaller diameter first passes compared to the 5 larger diameter first passes of the base case, increases the available surface area for heat transfer. The fuel flow rate is decreased by 3% to realize a constant propene to ethene ratio. This results in lower heat fluxes and tube metal temperatures on the second pass since a larger percentage of the total heat is absorbed by the larger number of first passes in the altered geometry. As the alternative reactor design requires a staggered configuration of the coils in the firebox, larger circumferential tube metal temperature differences are observed. The olefin yields obtained in the alternative reactor design are lower: -0.6% and -0.1% relative to the base case for ethene and propene

respectively. The run length increases by 82% while the CO<sub>2</sub> emission per ton ethene produced slightly decreases.

Finally, the influence of the excess bridgewall oxygen concentration is examined. An increased excess oxygen concentration of 2.8 vol% compared to 1.9 vol% in the base case requires 6.4% extra fuel and 5.5% extra combustion air to maintain the cracking severity. This non-negligible increase in fuel flow makes the excess oxygen concentration the most important performance indicator of the furnace to control when aiming for a furnace efficiency increase and CO<sub>2</sub> emission reduction. Its control also requires no or very limited adaptation to the furnace compared to the implementation of a coating or a new reactor coil.

All operational changes and technologies studied in this work can be combined to further minimize the CO<sub>2</sub> emissions, but controlling and monitoring of the excess bridgewall oxygen is crucial to realize a reduction in CO<sub>2</sub> emissions for an existing unaltered furnace.

## Acknowledgements

Florian Wéry and Moreno Geerts acknowledge financial support from a doctoral fellowship from the Fund for Scientific Research Flanders (FWO) under application number 1S97521N, 1248922N and by the Baekeland mandate HBC.2016.0594. The computational resources (Stevin Supercomputer Infrastructure) and services used in this work were provided by the VSC (Flemish Supercomputer Center), funded by Ghent University, FWO and the Flemish Government – department EWI. The research leading to these results has also received funding from the European Research Council (ERC) under the H2020 grant agreement no. 818607 (OPTIMA).

## Nomenclature

### Roman

$A$	Cross-sectional surface area	$m^2$
$c$	Model constant	—
$C_p$	Specific heat capacity	$J\ kg^{-1}K^{-1}$
$C_{p,m}$	Molar heat capacity	$J\ mol^{-1}K^{-1}$
$d$	Diameter	$m$
$D$	Diffusion coefficient	$m^2\ s^{-1}$
$f$	Fanning friction factor	—
$F$	Molar flow rate	$mol\ s^{-1}$
$g$	Gravitational constant	$m\ s^{-2}$
$h$	Molar enthalpy	$J\ mol^{-1}$
$H$	Specific enthalpy	$J\ kg^{-1}$
$I_\lambda$	Spectral intensity	$W\ sr^{-1}\ m^{-1}$
$J^H$	Enthalpy flux	$W\ m^{-2}$
$J^Z$	Mass flux	$kg\ m^{-2}\ s^{-1}$
$k$	Thermal conductivity	$W\ m^{-1}\ K^{-1}$
$k$	Turbulent kinetic energy	$m^2\ s^{-2}$
$L$	Length	$m$
$p$	Pressure	$Pa$
$\dot{q}$	Heat flux	$W\ m^{-2}$
$r$	Radius	$m$
$r$	Volumetric reaction rate	$mol\ m^{-3}\ s^{-1}$
$R$	Net production rate	$mol\ m^{-3}\ s^{-1}$
$t$	Time	$s$
$T$	Temperature	$K$

$u$	Velocity	$m s^{-1}$
$U$	Heat transfer coefficient	$W m^{-2} K^{-1}$
$w$	Weight factor	—
$z$	Axial coordinate	$m$
$Z$	Mixture fraction	—

### Greek

$\varepsilon$	Turbulent dissipation rate	$m^2 s^{-3}$
$\varepsilon$	Emissivity	—
$\zeta$	Nekrasov factor for tube bends	—
$\eta$	Efficiency	—
$\kappa_\lambda$	Spectral absorption coefficient	—
$\lambda$	Wavelength	$m$
$\mu$	Dynamic viscosity	$Pa s$
$\nu$	Stoichiometric coefficient	—
$\rho$	Density	$kg m^{-3}$
$\sigma_t$	Turbulent Prandtl number	—
$\bar{\tau}$	Viscous stress tensor	$kg m^{-1} s^{-2}$
$\chi$	Scalar dissipation rate	$s^{-1}$
$\omega$	Circumference	$m$

### Sub/superscripts

b	Blackbody
c	Coking
f	Fuel
g	Gas
H	Enthalpy
i	Index

o	Oxidizer
t	Turbulent
Z	Mixture fraction
,	Variance
~	Favre-averaged value

### Acronyms

BWT	Bridgewall temperature
CFD	Computational Fluid Dynamics
CIP	Coil inlet pressure
CIT	Coil inlet temperature
COT	Coil outlet temperature
DOM	Discrete ordinates model
IRHF	Incident radiative heat flux
ODE	Ordinary differential equation
P/E ratio	Propene to ethene ratio
RNG	Re-Normalisation Group
RTE	Radiative transfer equation
SIMPLE	Semi-implicit method for pressure-linked equation
TLE	Transfer line exchanger
TMT	Tube metal temperatures
WSGGM	Weighted sum of gray gas models

## References

- [1] I. Amghizar, J. Dedeayne, D.J. Brown, G.B. Marin, K.M. Van Geem, Sustainable innovations in steam cracking: CO<sub>2</sub> neutral olefin production, *React. Chem. Eng.* 5 (2020) 239-257. doi.org/10.1039/c9re00398c.
- [2] Y. Gao, L. Neal, D. Ding, W. Wu, C. Baroi, A.M. Gaffney, F. Li, Recent Advances in Intensified Ethylene Production—A Review, *ACS Catal.* 9 (2019) 8592-8621. doi.org/10.1021/acscatal.9b02922.
- [3] Z. Zhao, J. Jiang, F. Wang, An economic analysis of twenty light olefin production pathways, *J. Energy Chem.* 56 (2021) 193-202. doi.org/10.1016/j.jechem.2020.04.021.
- [4] L. Berkelaar, J.v.d. Linde, J. Peper, A. Rajhans, D. Tiemessen, L.v.d. Ham, H.v.d. Berg, Electrochemical conversion of carbon dioxide to ethylene: Plant design, evaluation and prospects for the future, *Chem. Eng. Res. Des.* 182 (2022) 194-206. doi.org/10.1016/j.cherd.2022.03.034.
- [5] K.M. Van Geem, V.V. Galvita, G.B. Marin, Making chemicals with electricity, *Science* 364 (2019) 734-735. 10.1126/science.aax5179.
- [6] T. Ren, M. Patel, K. Blok, Olefins from conventional and heavy feedstocks: Energy use in steam cracking and alternative processes, *Energy* 31 (2006) 425-451. 10.1016/j.energy.2005.04.001.
- [7] T. Ren, M.K. Patel, K. Blok, Steam cracking and methane to olefins: Energy use, CO<sub>2</sub> emissions and production costs, *Energy* 33 (2008) 817-833. 10.1016/j.energy.2008.01.002.
- [8] M.W.M. van Goethem, S. Barendregt, J. Grievink, P.J.T. Verheijen, M. Dente, E. Ranzi, A kinetic modelling study of ethane cracking for optimal ethylene yield, *Chem. Eng. Res. Des.* 91 (2013) 1106-1110. doi.org/10.1016/j.cherd.2013.01.006.
- [9] P. Friedlingstein, M. O'Sullivan, M.W. Jones, R.M. Andrew, J. Hauck, A. Olsen, G.P. Peters, W. Peters, J. Pongratz, S. Sitch, C. Le Quéré, J.G. Canadell, P. Ciais, R.B. Jackson, S. Alin, L.E.O.C. Aragão, A. Arneeth, V. Arora, N.R. Bates, M. Becker, A. Benoit-Cattin, H.C. Bittig, L. Bopp, S. Bultan, N. Chandra, F. Chevallier, L.P. Chini, W. Evans, L. Florentie, P.M. Forster, T. Gasser, M. Gehlen, D. Gilfillan, T. Gkritzalis, L. Gregor, N. Gruber, I. Harris, K. Hartung, V. Haverd, R.A. Houghton, T. Ilyina, A.K. Jain, E. Joetzjer, K. Kadono, E. Kato, V. Kitidis, J.I. Korsbakken, P. Landschützer, N. Lefèvre, A. Lenton, S. Lienert, Z. Liu, D. Lombardozzi, G. Marland, N. Metz, D.R. Munro, J.E.M.S. Nabel, S.I. Nakaoka, Y. Niwa, K. O'Brien, T. Ono, P.I. Palmer, D. Pierrot, B. Poulter, L. Resplandy, E. Robertson, C. Rödenbeck, J. Schwinger, R.

Séférian, I. Skjelvan, A.J.P. Smith, A.J. Sutton, T. Tanhua, P.P. Tans, H. Tian, B. Tilbrook, G. van der Werf, N. Vuichard, A.P. Walker, R. Wanninkhof, A.J. Watson, D. Willis, A.J. Wiltshire, W. Yuan, X. Yue, S. Zaehle, Global Carbon Budget 2020, *Earth Syst. Sci. Data* 12 (2020) 3269-3340. [10.5194/essd-12-3269-2020](https://doi.org/10.5194/essd-12-3269-2020).

[10] G.F. Glasier, P.D. Pacey, Formation of pyrolytic carbon during the pyrolysis of ethane at high conversions, *Carbon* 39 (2001) 15-23. [10.1016/S0008-6223\(00\)00079-8](https://doi.org/10.1016/S0008-6223(00)00079-8).

[11] S. Mahamulkar, K. Yin, P.K. Agrawal, R.J. Davis, C.W. Jones, A. Malek, H. Shibata, Formation and Oxidation/Gasification of Carbonaceous Deposits: A Review, *Ind. Eng. Chem. Res.* 55 (2016) 9760-9818. [doi.org/10.1021/acs.iecr.6b02220](https://doi.org/10.1021/acs.iecr.6b02220).

[12] K.M. Van Geem, I. Dhuyvetter, S. Prokopiev, M.F. Reyniers, D. Viennet, G.B. Marin, Coke Formation in the Transfer Line Exchanger during Steam Cracking of Hydrocarbons, *Ind. Eng. Chem. Res.* 48 (2009) 10343-10358. [doi.org/10.1021/ie900124z](https://doi.org/10.1021/ie900124z).

[13] J. Wang, M.-F. Reyniers, G.B. Marin, Influence of Dimethyl Disulfide on Coke Formation during Steam Cracking of Hydrocarbons, *Ind. Eng. Chem. Res.* 46 (2007) 4134-4148. [doi.org/10.1021/ie061096u](https://doi.org/10.1021/ie061096u).

[14] J. Wang, M.-F. Reyniers, K.M. Van Geem, G.B. Marin, Influence of Silicon and Silicon/Sulfur-Containing Additives on Coke Formation during Steam Cracking of Hydrocarbons, *Ind. Eng. Chem. Res.* 47 (2008) 1468-1482. [doi.org/10.1021/ie070970w](https://doi.org/10.1021/ie070970w).

[15] M.W.M. van Goethem, E. Jelsma, Numerical and experimental study of enhanced heat transfer and pressure drop for high temperature applications, *Chem. Eng. Res. Des.* 92 (2014) 663-671. [doi.org/10.1016/j.cherd.2014.02.009](https://doi.org/10.1016/j.cherd.2014.02.009).

[16] R. Campet, M. Zhu, E. Riber, B. Cuenot, M. Nemri, Large Eddy Simulation of a single-started helically ribbed tube with heat transfer, *Int. J. Heat Mass Transfer* 132 (2019) 961-969. [doi.org/10.1016/j.ijheatmasstransfer.2018.11.163](https://doi.org/10.1016/j.ijheatmasstransfer.2018.11.163).

[17] Y. Zong, D. Bai, M. Zhou, L. Zhao, Numerical studies on heat transfer enhancement by hollow-cross disk for cracking coils, *Chem. Eng. Process.* 135 (2019) 82-92. [doi.org/10.1016/j.cep.2018.11.007](https://doi.org/10.1016/j.cep.2018.11.007).

[18] Z. Zhang, L.F. Albright, Pretreatments of Coils to Minimize Coke Formation in Ethylene Furnaces, *Ind. Eng. Chem. Res.* 49 (2010) 1991-1994. [doi.org/10.1021/ie900271q](https://doi.org/10.1021/ie900271q).

[19] D.J. Van Cauwenberge, C.M. Schietekat, J. Floré, K.M. Van Geem, G.B. Marin, CFD-based design of 3D pyrolysis reactors: RANS vs. LES, *Chem. Eng. J.* 282 (2015) 66-76. doi.org/10.1016/j.cej.2015.03.020.

[20] S. Vangaever, P.A. Reyniers, S.H. Symoens, N.D. Ristic, M.R. Djokic, G.B. Marin, K.M. Van Geem, Pyrometer-based control of a steam cracking furnace, *Chem. Eng. Res. Des.* 153 (2020) 380-390. doi.org/10.1016/j.cherd.2019.10.023.

[21] J.N. Dedeyne, D.J. Van Cauwenberge, P.A. Reyniers, K.M. Van Geem, G.B. Marin, Large eddy simulation of tubular reactors with spherical dimples, *Chemical Engineering Journal* 380 (2020) 122463. 10.1016/j.cej.2019.122463.

[22] C.M. Schietekat, M.W.M. van Goethem, K.M. Van Geem, G.B. Marin, Swirl flow tube reactor technology: An experimental and computational fluid dynamics study, *Chem. Eng. J.* 238 (2014) 56-65. doi.org/10.1016/j.cej.2013.08.086.

[23] L.A. Vandewalle, D.J. Van Cauwenberge, J.N. Dedeyne, K.M. Van Geem, G.B. Marin, Dynamic simulation of fouling in steam cracking reactors using CFD, *Chem. Eng. J.* 329 (2017) 77-87. doi.org/10.1016/j.cej.2017.06.113.

[24] S. Vangaever, J. Van Thielen, J. Hood, J. Olver, P. Honnerová, G.J. Heynderickx, K.M. Van Geem, The Effect of Refractory Wall Emissivity on the Energy Efficiency of a Gas-Fired Steam Cracking Pilot Unit, *Materials* 14 (2021). 10.3390/ma14040880.

[25] S. Vangaever, P.A. Reyniers, C. Visser, D. Jakobi, G.J. Heynderickx, G.B. Marin, K.M. Van Geem, Computational Fluid Dynamics-Based Study of a High Emissivity Coil Coating in an Industrial Steam Cracker, *Ind. Eng. Chem. Res.* 57 (2018) 16782-16794. doi.org/10.1021/acs.iecr.8b04068.

[26] C. Herce, A. González-Espinosa, A. Gil, C. Cortés, J. González-Rebordinos, T. Guégués, M. Gil, L. Ferré, F. Brunet, A. Arias, Combustion monitoring in an industrial cracking furnace based on combined CFD and optical techniques, *Fuel* 280 (2020) 118502. 10.1016/j.fuel.2020.118502.

[27] S. Gong, C. Shao, L. Zhu, An energy efficiency integration optimization scheme for ethylene production with respect to multiple working conditions, *Energy* 182 (2019) 280-295. 10.1016/j.energy.2019.06.035.

[28] O. Mynko, I. Amghizar, D.J. Brown, L. Chen, G.B. Marin, R.F. de Alvarenga, D.C. Uslu, J. Dewulf, K.M. Van Geem, Reducing CO<sub>2</sub> emissions of existing ethylene plants: Evaluation of

different revamp strategies to reduce global CO<sub>2</sub> emission by 100 million tonnes, *J. Clean. Prod.* 362 (2022) 132127. doi.org/10.1016/j.jclepro.2022.132127.

[29] J. González Rebordinos, C. Herce, A. González-Espinosa, M. Gil, C. Cortés, F. Brunet, L. Ferré, A. Arias, Evaluation of retrofitting of an industrial steam cracking furnace by means of CFD simulations, *Appl. Therm. Eng.* 162 (2019) 114206. doi.org/10.1016/j.applthermaleng.2019.114206.

[30] Y. Zhang, F. Qian, Y. Zhang, C.M. Schietekat, K.M. Van Geem, a. Guy, G.B. Marin, Impact of flue gas radiative properties and burner geometry in furnace simulations, *AIChE J.* 61 (2015) 936-954. doi.org/10.1002/aic.14724.

[31] G.D. Stefanidis, B. Merci, G.J. Heynderickx, G.B. Marin, Gray/nongray gas radiation modeling in steam cracker CFD calculations, *AIChE J.* 53 (2007) 1658-1669. doi.org/10.1002/aic.11186.

[32] G.D. Stefanidis, B. Merci, G.J. Heynderickx, G.B. Marin, CFD simulations of steam cracking furnaces using detailed combustion mechanisms, *Comput. Chem. Eng.* 30 (2006) 635-649. doi.org/10.1016/j.compchemeng.2005.11.010.

[33] B. Mayr, R. Prieler, M. Demuth, C. Hochenauer, The usability and limits of the steady flamelet approach in oxy-fuel combustions, *Energy* 90 (2015) 1478-1489. doi.org/10.1016/j.energy.2015.06.103.

[34] K. Bray, Laminar Flamelets in Turbulent Combustion Modeling, *Combust. Sci. Technol.* 188 (2016) 1372-1375. doi.org/10.1080/00102202.2016.1195819.

[35] H.C. Hottel, A.F. Sarofim, Radiative transfer, McGraw-Hill Book Company, New York (1967)

[36] W. Zhou, T. Qiu, Zone modeling of radiative heat transfer in industrial furnaces using adjusted Monte-Carlo integral method for direct exchange area calculation, *Appl. Therm. Eng.* 81 (2015) 161-167. doi.org/10.1016/j.applthermaleng.2015.02.004.

[37] W.P. Jones, J.H. Whitelaw, Calculation methods for reacting turbulent flows: A review, *Combust. Flame* 48 (1982) 1-26. doi.org/10.1016/0010-2180(82)90112-2.

[38] V. Yakhot, S.A. Orszag, S. Thangam, T.B. Gatski, C.G. Speziale, Development of turbulence models for shear flows by a double expansion technique, *Phys. Fluids A* 4 (1992) 1510-1520. doi.org/10.1063/1.858424.

- [39] D.M.G. Gregory P. Smith, Michael Frenklach, Nigel W. Moriarty, Boris Eiteneer, Mikhail Goldenberg, C. Thomas Bowman, Ronald K. Hanson, Soonho Song, William C. Gardiner, Jr., Vitali V. Lissianski, and Zhiwei Qin, [http://www.me.berkeley.edu/gri\\_mech/](http://www.me.berkeley.edu/gri_mech/)
- [40] H. Pitsch, H. Barths, N. Peters, Three-Dimensional Modeling of NO<sub>x</sub> and Soot Formation in DI-Diesel Engines Using Detailed Chemistry Based on the Interactive Flamelet Approach, (1996). 10.4271/962057.
- [41] H. Pitsch, N. Peters, A Consistent Flamelet Formulation for Non-Premixed Combustion Considering Differential Diffusion Effects, *Combust. Flame* 114 (1998) 26-40. doi.org/10.1016/S0010-2180(97)00278-2.
- [42] B. Marracino, D. Lentini, Radiation Modelling in Non-Luminous Nonpremixed Turbulent Flames, *Combust. Sci. Technol.* 128 (1997) 23-48. doi.org/10.1080/00102209708935703.
- [43] S.R. Mathur, J.Y. Murthy, Coupled Ordinates Method for Multigrid Acceleration of Radiation Calculations, *J. Thermophys. Heat Transfer* 13 (1999) 467-473. doi.org/10.2514/2.6485.
- [44] G.D. Raithby, E.H. Chui, A Finite-Volume Method for Predicting a Radiant Heat Transfer in Enclosures With Participating Media, *J. Heat Transfer* 112 (1990) 415-423. doi.org/10.1115/1.2910394.
- [45] T.F. Smith, Z.F. Shen, J.N. Friedman, Evaluation of Coefficients for the Weighted Sum of Gray Gases Model, *J. Heat Transfer* 104 (1982) 602-608. doi.org/10.1115/1.3245174.
- [46] T.F. Smith, Z.F. Shen, J.N. Friedman, Evaluation of Coefficients for the Weighted Sum of Gray Gases Model, *Journal of Heat Transfer* 104 (1982) 602-608. 10.1115/1.3245174.
- [47] Y. Ren, G. Guo, Z. Liao, Y. Yang, J. Sun, B. Jiang, J. Wang, Y. Yang, Kinetic modeling with automatic reaction network generator, an application to naphtha steam cracking, *Energy* 207 (2020) 118204. 10.1016/j.energy.2020.118204.
- [48] K.M. Van Geem, M.F. Reyniers, G.B. Marin, Challenges of Modeling Steam Cracking of Heavy Feedstocks, *Oil Gas Sci. Technol.* 63 (2008) 79-94. doi.org/10.2516/ogst:2007084.

- [49] K.M. Van Geem, D. Hudebine, M.F. Reyniers, F. Wahl, J.J. Verstraete, G.B. Marin, Molecular reconstruction of naphtha steam cracking feedstocks based on commercial indices, *Comput. Chem. Eng.* 31 (2007) 1020-1034. doi.org/10.1016/j.compchemeng.2006.09.001.
- [50] K.M. Van Geem, G.J. Heynderickx, G.B. Marin, Effect of radial temperature profiles on yields in steam cracking, *AIChE J.* 50 (2004) 173-183. doi.org/10.1002/aic.10016.
- [51] M.K. Sabbe, K.M. Van Geem, M.-F. Reyniers, G.B. Marin, First principle-based simulation of ethane steam cracking, *AIChE J.* 57 (2011) 482-496. doi.org/10.1002/aic.12269.
- [52] Y. Zhang, P.A. Reyniers, W. Du, F. Qian, K.M. Van Geem, G.B. Marin, Incident Radiative Heat Flux Based Method for the Coupled Run Length Simulation of Steam Cracking Furnaces, *Ind. Eng. Chem. Res.* 56 (2017) 4156-4172. doi.org/10.1021/acs.iecr.6b05013.
- [53] P.M. Plehiers, G.C. Reyniers, G.F. Froment, Simulation of the run length of an ethane cracking furnace, *Ind. Eng. Chem. Res.* 29 (1990) 636-641. doi.org/10.1021/ie00100a022.
- [54] G.J. Heynderickx, G.F. Froment, A Pyrolysis Furnace with Reactor Tubes of Elliptical Cross Section, *Ind. Eng. Chem. Res.* 35 (1996) 2183-2189. doi.org/10.1021/ie9504009.
- [55] G.D. Stefanidis, K.M. Van Geem, G.J. Heynderickx, G.B. Marin, Evaluation of high-emissivity coatings in steam cracking furnaces using a non-grey gas radiation model, *Chem. Eng. J.* 137 (2008) 411-421. doi.org/10.1016/j.cej.2007.04.042.